

# Statistical analysis on X-ray flares from the nucleus and HST-1 knot in the M87 jet

Shenbang Yang,<sup>1</sup> Dahai Yan,<sup>2,3\*</sup> Benzhong Dai,<sup>1†</sup> Pengfei Zhang,<sup>1</sup> Qianqian Zhu,<sup>4</sup>

Jiancheng Wang,<sup>2,3</sup> and Li Zhang<sup>1</sup>

<sup>1</sup>Key Laboratory of Astroparticle Physics of Yunnan Province, Yunnan University, Kunming 650091, China

<sup>2</sup>Key Laboratory for the Structure and Evolution of Celestial Objects, Yunnan Observatory, Chinese Academy of Sciences, Kunming 650011, China

<sup>3</sup>Center for Astronomical Mega-Science, Chinese Academy of Sciences, 20A Datun Road, Chaoyang District, Beijing 100012, China

<sup>4</sup>Department of General Studies, Nanchang Institute of Science & Technology, Nanchang 330108, China

Accepted XXX. Received YYY; in original form ZZZ

## ABSTRACT

The statistical properties of X-ray flares from two separate locations (nucleus and HST-1) in the M87 jet are investigated to reveal the physical origin of the flares. We analyse the archival *Chandra* data for M87, and identify 14 flares in the nucleus and 9 flares in HST-1. The peak intensity ( $I_p$ ) and the flaring duration time ( $T_{\text{fl}}$ ) for each flare are obtained. It is found that the distributions of both  $I_p$  and  $T_{\text{fl}}$  for the nucleus obey a power-law form with a similar index. A similar result is also obtained for HST-1, and no significant inconsistency between the nucleus and HST-1 is found for the indices. Similar to solar X-ray flares, the power-law distributions of the flare event parameters can be well explained by a self-organized criticality (SOC) system, which are triggered by magnetic reconnection. Our results suggest that the flares from nucleus and HST-1 are possibly triggered by magnetic reconnection process. The consistent indices for the distributions of  $I_p$  and  $T_{\text{fl}}$  in the CORE and HST-1 indicate that the dimensions of the energy dissipation of the magnetic reconnection is identical in the two regions. A strong correlation between the flares in the two regions also suggests a similar physical origin for the flares.

**Key words:** galaxies: jets – X-rays: individuals: M87 – radiation mechanisms: non-thermal

## 1 INTRODUCTION

Active galactic nucleus (AGN) is believed to host a super-massive black hole (SMBH), which might be the central engine powering a powerful jet. M87 is a radio galaxy with a central SMBH of about  $3 - 6 \times 10^9 M_{\odot}$  (e.g., Macchetto et al. 1997; Gebhardt & Thomas 2009) and a collimated jet misaligned by  $\sim 30^\circ$  with respect to the line of sight (e.g., Biretta et al. 1995). The nucleus (hereafter, CORE) and several knots in the jet are exposed at radio, optical, and X-ray wavelengths. Apart from the CORE, the most interesting X-ray emission region is the inner knot HST-1, which is  $\sim 1''$  from the CORE, and was first discussed by Biretta et al. (1999) for the optical region.

Thanks to the unprecedented resolution of *Chandra*, which is  $\leq 0''.5$  (Weisskopf et al. 2000), the high energy radiation mechanisms in substructures in the M87 jet have been

studied in detail. The X-ray emissions from the CORE and HST-1 are believed to be dominated by non-thermal synchrotron radiation (e.g., Marshall et al. 2002; Wilson & Yang 2002; Zhang et al. 2010; Sun et al. 2018). Strong flares from the two regions are detected, and the variability timescales span from months to years (Harris et al. 2003; Perlman et al. 2003; Harris et al. 2006).

The physical origin of the X-ray flares is not well understood. Rather than the conventional view that jet emissions are powered by shocks, Sironi et al. (2015) suggested that the magnetic reconnection process powers jet emissions. Numerical simulations have been performed to test this mechanism, and the results indicated that the variability in AGNs or  $\gamma$ -ray bursts (GRBs) can be explained with the fast magnetic reconnection process driven by kink-instability turbulence (Singh et al. 2016).

The flares triggered by magnetic reconnection are presumed to form a self-organized criticality (SOC) system, such as solar flares (e.g., Lu & Hamilton 1991; Aschwanden 2011). The SOC system predicts that the event parameters,

\* E-mail: yandahai@ynao.ac.cn

† E-mail: bzhdai@ynu.edu.cn

including peak flux and flaring time duration, follow power-law distributions, and the corresponding indices are related to the effective geometric dimension of the system (e.g., [Aschwanden 2012](#)). The SOC model has been proposed to explain the statistical properties of the X-ray flares from GRBs ([Wang & Dai 2013](#); [Yi et al. 2016](#)), blazars ([Yan et al. 2018](#)), M87 ([Wang et al. 2015](#)), and Sgr A\* ([Wang et al. 2015](#); [Li et al. 2015](#); [Yuan et al. 2018](#)).

By employing *Chandra* data, [Wang et al. \(2015\)](#) investigated the statistical properties of 18 flares from the nucleus of the M87 jet, and claimed that those properties can be explained by an SOC model. Besides the nucleus, HST-1 is another bright X-ray emission region in the M87 jet. The *Chandra* observations facilitate the study of X-ray flares from different regions in the M87 jet.

We focus on the X-ray flares from the nucleus and HST-1 in the M87 jet, exploring the statistical properties of the X-ray flares from the two regions. This enables us to make a comparison between the energy dissipation mechanisms in the two regions. This paper is organized as following: the *Chandra* data reduction process is described in Sect. 2, and the results are presented in Sect. 3. The a discussion and conclusions are provided in Sect. 4.

## 2 DATA REDUCTION AND ANALYSIS

Until January 2019, M87 has been observed 122 times by *Chandra*. The data of 120 archival observations has been publicly released, and the observations are obtained by using the Advanced CCD Imaging Spectrometer (ACIS) with a 0.4s/3.2s frame time and using the High Resolution Camera (HRC). To minimize pile-up effects, we reprocessed 105 archival observations with a 0.4 s frame time (e.g., [Harris et al. 2006](#)) from the *Chandra* Data Archive (CDA)<sup>1</sup>. These observations are all imaged by ACIS. The information for these observations are listed in Table 1. We perform the data reduction procedures using *Chandra* Interactive Analysis of Observations (CIAO, v4.10) and the *Chandra* Calibration Database (CALDB, v4.7.8).

However, a series of studies on the M87 jet using *Chandra* data demonstrated that some observations with a 0.4 s frame still suffered from pile-up effects, especially for those of HST-1 in an outburst around 2005 ([Harris et al. 2006, 2009, 2011](#)). The pile-up effect arises when two or more photons are detected by a CCD in a frame time, within a single pixel ([Davis 2001](#)). If an observation of a bright source is affected by the heavy pile-up, the spectrum is distorted so that the original spectral information and integral energy flux can not be obtained. To recover the intensity of the piled source, [Harris et al. \(2006\)](#) proposed the “keV s<sup>-1</sup>” method that extracts the observed intensity of the source in an evt1 file without any grade filtering. This method is the most efficient way to restore the intrinsic variability of a piled source, although some unrecoverable effects, such as “Eat Thy Neighbor”, “second-order effects of pileup” (see [Harris et al. \(2009\)](#) for details), can probably induce deviation in the intensity of the source. We, therefore, use the “keV s<sup>-1</sup>” method to estimate the total observed intensities

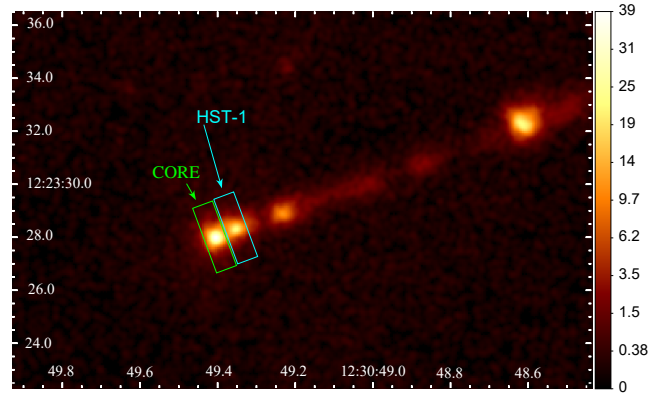


**Figure 1.** Image of the observation 1808, binned in 0.123 arcsec per pixel. The x-axis is the right ascension, and the y-axis is the declination. The green and cyan rectangle of length 2.6 arcsec transverse to the jet and 0.8 arcsec along the jet are the selected source regions for the CORE and HST-1, respectively, in the data reduction.

in the CORE and HST-1 following the procedures in [Harris et al. \(2006\)](#). For convenience, we use the CIAO tool `dmstat` to obtain the total energy (in units of eV) of all events on the evt1 files within the rectangular regions of length 2.6 arcsec transverse to the jet and 0.8 arcsec along the jet, as shown in Fig. 1. To separate the CORE from HST-1, [Harris et al. \(2006\)](#) selected a circular region with radius of 0.44 arcsec for HST-1. We extract the events from a rectangle with length 0.8 arcsec along the jet (i.e., 0.4 arcsec along the jet from the centre of the source) to avoid contamination by the adjacent source. Henceforth, the intensities can be calculated by  $total\ energy/exposure/1000$ , and the results are listed in Table 1. Statistical uncertainties can be calculated based on the counts:  $\sqrt{N}/N$ , and they are negligible in our analyses since they range from 1 to 5%, according to [Harris et al. \(2009\)](#). Only the standard good-time intervals are applied to the evt1 files.

Furthermore, we examine the possible contamination between the two regions with the point spread function (PSF) simulations, using the software MARX<sup>2</sup>. We first calculate the encircled counts fraction (ECF) within a circle of 0.4 arcsec radius for the CORE and HST-1 in observation 1808. Then we separately simulate the CORE and HST-1 for the same observation with MARX, and then calculate their ECF within same radius circle. The results are displayed in Figure 2. If the source in the region of 0.4 arcsec radius is contaminated by the adjacent source, the observed ECF of this source will be distorted. An apparent discrepancy will then be revealed between the observed and simulated ECF in this case. Nevertheless, it has been found that there is no obvious discrepancy in our results, and the contamination is negligible.

<sup>1</sup> <http://asc.harvard.edu/cda/>

<sup>2</sup> <https://space.mit.edu/ASC/MARX/>

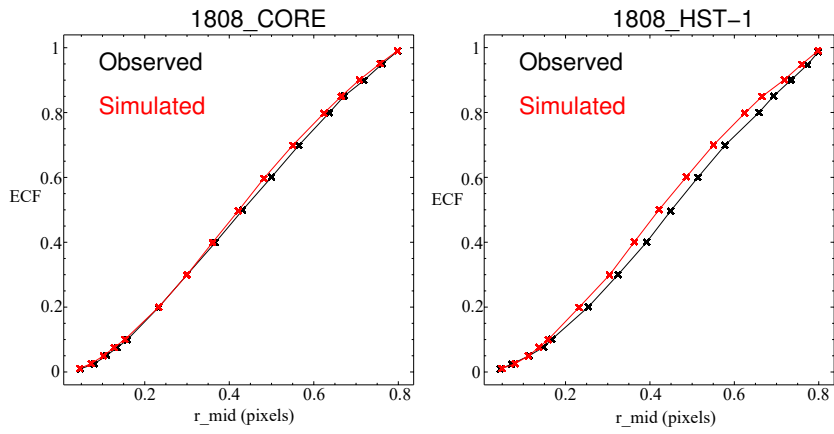


**Figure 2.** The observed and simulated ECF of the CORE and HST-1 in observation 1808. Variable  $r_{\text{mid}}$  is the radius from the coordinate of the corresponding source.

Table 1: Observational information for M87 and the results of data analysis. (1) Observation ID, (2,3) the start time of the observation, (4) total exposure, (5,6) observed intensity of the CORE and HST-1, respectively, in units of keV s<sup>-1</sup>. It is extracted from the regions shown in Fig. 1. No background is subtracted.

Obs.ID	Time		Expo. (ks)	the CORE	HST-1
	UT	MJD		<i>I</i>	<i>I</i>
(1)	(2)	(3)	(4)	(5)	(6)
1808	2000-07-30T20:42:04	51755.8626	12.85	0.33	0.19
3085	2002-01-16T01:25:51	52290.0596	4.89	0.69	0.62
3084	2002-02-12T09:03:18	52317.3773	4.66	0.59	0.5
3086	2002-03-30T07:36:53	52363.3173	4.62	0.66	0.43
3087	2002-06-08T19:58:05	52433.832	4.97	0.47	0.74
3088	2002-07-24T14:20:38	52479.5977	4.71	0.58	0.99
3975	2002-11-17T02:25:39	52595.1012	5.29	0.7	0.7
3976	2002-12-29T14:13:52	52637.593	4.79	0.67	0.58
3977	2003-02-04T14:22:12	52674.5988	5.28	0.62	0.57
3978	2003-03-09T21:20:35	52707.8893	4.85	0.82	0.77
3979	2003-04-14T05:46:54	52743.2409	4.49	0.64	0.99
3980	2003-05-18T22:11:43	52777.9248	4.79	0.42	0.97
3981	2003-07-03T09:13:36	52823.3845	4.68	0.44	0.84
3982	2003-08-08T04:28:37	52859.1866	4.84	0.31	1.25
4917	2003-11-11T19:46:06	52954.8237	5.03	0.91	2.01
4918	2003-12-29T09:45:40	53002.4067	4.68	0.51	1.91
4919	2004-02-12T05:27:42	53047.2276	4.7	0.83	3.85
4921	2004-05-13T03:40:04	53138.1528	5.25	0.85	4.87
4922	2004-06-23T18:26:35	53179.7685	4.54	0.43	5.48
4923	2004-08-05T08:11:51	53222.3416	4.63	0.56	5.66
5737	2004-11-26T20:19:16	53335.8467	4.21	1.46	6.82
5738	2005-01-24T01:42:58	53394.0715	4.67	1.55	7.69
5739	2005-02-14T18:44:29	53415.7809	5.15	1.75	8.11
5740	2005-04-22T16:20:31	53482.6809	4.7	1.2	11.5
5744	2005-04-28T14:01:45	53488.5846	4.7	1.04	11.87
5745	2005-05-04T22:58:04	53494.957	4.71	1.18	11.15
5746	2005-05-13T01:51:28	53503.0774	5.14	1.07	11.2
5747	2005-05-22T03:20:36	53512.1393	4.7	0.94	11.09
5748	2005-05-30T02:31:18	53520.1051	4.7	0.86	10.08
5741	2005-06-03T03:31:43	53524.147	4.7	0.86	9.39
5742	2005-06-21T01:39:21	53542.069	4.7	0.71	9.78
5743	2005-08-06T17:33:28	53588.7316	4.67	0.39	7.14
6299	2005-11-29T02:01:54	53703.0847	4.66	0.68	3.65
6300	2006-01-05T03:08:49	53740.1311	4.66	0.8	3.55
6301	2006-02-19T23:36:31	53785.9837	4.34	1.05	3.4
6302	2006-03-30T09:25:20	53824.3926	4.7	0.52	3.8
6303	2006-05-21T16:22:42	53876.6824	4.7	0.55	3.05
6304	2006-06-28T14:07:05	53914.5883	4.68	1.36	2.37
6305	2006-08-02T20:52:12	53949.8696	4.65	0.98	2.04
7348	2006-11-13T16:54:29	54052.7045	4.54	0.83	4.11
7349	2007-01-04T02:09:51	54104.0902	4.68	0.85	3.55
7350	2007-02-13T06:56:01	54144.2889	4.66	0.96	3.59
8510	2007-02-15T09:08:50	54146.3811	4.7	0.8	3.48
8511	2007-02-18T22:05:59	54149.9208	4.7	0.71	3.64
8512	2007-02-21T23:46:51	54152.9909	4.7	0.87	3.29
8513	2007-02-24T03:02:04	54155.1264	4.7	0.94	3.31
8514	2007-03-12T11:32:42	54171.481	4.47	0.95	3.26
8515	2007-03-14T14:21:22	54173.5982	4.7	0.82	3.55
8516	2007-03-19T10:21:35	54178.4317	4.68	1.02	3.28
8517	2007-03-22T03:48:57	54181.159	4.67	1.02	3.38
7351	2007-03-24T19:24:42	54183.8088	4.68	0.97	3.58
7352	2007-05-15T11:01:49	54235.4596	4.59	0.56	3.0

Table 1: continued.

Obs.ID	Time		Expo. (ks)	the CORE <i>I</i>	HST-1 <i>I</i>
	UT	MJD			
(1)	(2)	(3)	(4)	(5)	(6)
7353	2007-06-25T14:10:22	54276.5905	4.54	0.5	3.35
7354	2007-07-31T01:30:37	54312.0629	4.71	0.38	3.52
8575	2007-11-25T17:03:03	54429.7105	4.68	0.66	1.33
8576	2008-01-04T23:07:16	54469.9634	4.69	0.69	1.19
8577	2008-02-16T11:30:12	54512.4793	4.66	1.55	1.15
8578	2008-04-01T19:38:16	54557.8182	4.71	0.86	1.37
8579	2008-05-15T04:26:06	54601.1848	4.71	0.65	1.32
8580	2008-06-24T06:27:54	54641.2694	4.7	1.12	1.15
8581	2008-08-07T18:46:52	54685.7826	4.66	0.46	0.94
10282	2008-11-17T22:34:25	54787.9406	4.7	0.4	0.55
10283	2009-01-07T09:12:03	54838.3834	4.71	0.45	0.52
10284	2009-02-20T22:38:07	54882.9431	4.7	0.43	0.45
10285	2009-04-01T07:15:18	54922.3023	4.66	0.44	0.4
10286	2009-05-13T22:43:11	54964.9467	4.68	0.53	0.38
10287	2009-06-22T11:23:53	55004.4749	4.7	0.57	0.33
10288	2009-12-15T20:12:58	55180.8423	4.68	0.67	0.29
11512	2010-04-11T21:14:39	55297.8852	4.7	1.26	0.32
11513	2010-04-13T14:16:43	55299.595	4.7	0.69	0.32
11514	2010-04-15T20:32:42	55301.856	4.53	0.57	0.31
11515	2010-04-17T21:47:42	55303.9081	4.7	0.61	0.32
11516	2010-04-20T13:20:52	55306.5562	4.71	0.59	0.33
11517	2010-05-05T19:25:21	55321.8093	4.7	0.71	0.29
11518	2010-05-09T02:39:49	55325.111	4.4	0.53	0.29
11519	2010-05-11T11:17:03	55327.4702	4.71	0.49	0.33
11520	2010-05-14T09:04:59	55330.3785	4.6	0.47	0.3
13964	2011-12-05T00:00:34	55900.0004	4.54	0.51	0.23
13965	2012-02-25T08:14:15	55982.3432	4.6	0.48	0.21
14974	2012-12-12T06:48:55	56273.284	4.6	0.43	0.14
14973	2013-03-12T04:44:30	56363.1976	4.4	0.44	0.16
16042	2013-12-26T15:15:16	56652.6356	4.62	0.31	0.13
16043	2014-04-02T14:37:46	56749.6096	4.6	0.52	0.13
17056	2014-12-17T18:31:58	57008.7722	4.6	0.37	0.1
17057	2015-03-19T19:58:41	57100.8324	4.6	0.49	0.1
18233	2016-02-23T12:39:14	57441.5273	37.25	0.2	0.07
18781	2016-02-24T10:05:22	57442.4204	39.52	0.2	0.07
18782	2016-02-26T00:58:57	57444.0409	34.07	0.23	0.07
18809	2016-03-12T04:45:53	57459.1985	4.52	0.23	0.06
18810	2016-03-13T07:09:25	57460.2982	4.6	0.21	0.08
18811	2016-03-14T13:26:22	57461.56	4.6	0.21	0.07
18812	2016-03-16T00:08:39	57463.006	4.4	0.22	0.07
18813	2016-03-17T03:27:17	57464.144	4.6	0.22	0.08
18783	2016-04-20T08:32:11	57498.3557	36.11	0.18	0.08
18232	2016-04-27T05:56:21	57505.2475	18.2	0.22	0.09
18836	2016-04-28T01:00:45	57506.0422	38.91	0.22	0.08
18837	2016-04-30T23:41:33	57508.9872	13.67	0.17	0.07
18838	2016-05-28T23:35:37	57536.9831	56.29	0.16	0.07
18856	2016-06-12T12:19:40	57551.5137	25.46	0.15	0.07
19457	2017-02-15T11:39:35	57799.4858	4.6	0.26	0.08
19458	2017-02-16T09:14:58	57800.3854	4.58	0.22	0.07
20034	2017-04-11T23:48:07	57854.9918	13.12	0.46	0.09
20035	2017-04-14T02:01:37	57857.0845	13.12	0.36	0.09
21075	2018-04-22T00:10:57	58230.0076	9.13	0.67	0.13
21076	2018-04-24T13:21:29	58232.5566	9.05	0.76	0.14

### 3 RESULTS

The light curves of the CORE and HST-1 are displayed in Figure 3. The intensities are similar to previous works (e.g., Harris et al. 2006) and Harris et al. (2009).

#### 3.1 Distributions of peak intensity and flaring time duration

We define a criteria that a “true” flare should experience a doubling or a halving of intensity, at least. This criterion could improve the significance of our analysis via filtering fake flares, which are produced by systematic uncertainties. Practically, we first mark the maximums of peaks and the minimums between neighbouring peaks in the light curves. Thereafter, we divide each peak intensity by the left and right adjacent minimums. When a value of  $\gtrsim 2$  ( $\geq 1.95$  in practice) is obtained, a “true” flare is identified. Ultimately, 14 flares for the CORE and 9 flares for HST-1 are identified through this procedure, and are listed in Table 2. We mark the flares identified only by the rising part with the character “r”, and the flares identified only by the declining part with the character “d”. The flares identified by both parts are labeled with the character “m”. All peak intensities ( $I_p$ ) of the flares can be directly read out. The flaring time durations ( $T_{\text{fl}}$ ) are calculated using the definition of  $T_{\text{fl}} = \text{EndTime} - \text{StartTime}$ .

Two models, a power-law model and a log-normal model, are used to fit the data. The reliable method for the estimation of the parameters of a statistic distribution model is Maximum likelihood (ML).

For a power-law distribution  $p(x) = A(\alpha, x_{\text{max}}, x_{\text{min}}) \cdot x^{-\alpha}$ , its logarithmic likelihood function can be expressed as

$$\ln L = -\alpha \sum_{i=1}^N \log(x_i) + N \cdot \log(A), \quad (1)$$

where the normalization coefficient  $A$  can be written as  $A = 1 - \alpha x_{\text{max}}^{1-\alpha} - x_{\text{min}}^{1-\alpha}$ . Specifically, when  $\alpha = 1$ ,  $A = 1/\log(x_{\text{max}}/x_{\text{min}})$ .

For a log-normal distribution,  $\mathcal{N}(\log x; \mu, \sigma)$ , the logarithmic likelihood function is

$$\ln L = -\frac{N}{2} \log(2\pi\sigma^2) - \sum_{i=1}^N \log(x_i) - \frac{1}{2\sigma^2} \sum_{i=1}^N (\log(x_i) - \mu)^2. \quad (2)$$

We use the Markov Chain Monte Carlo (MCMC) technique (e.g., Yan et al. 2013, 2015) to maximize the likelihood functions, and obtain the best-fit parameters of the power-law and log-normal models. The results are given in Table 3.

In Figure 4, we show the comparison of the data points and our best-fit results. Given the small number of the flares, we adopt the cumulative distribution. The results of the power-law model (dot-dashed lines) are calculated with  $N_{\text{PL}}(> x)$  and the corresponding best-fit parameters, where

$$N_{\text{PL}}(> x) = \frac{a}{\alpha - 1} (x^{1-\alpha} - x_{\text{max}}^{1-\alpha}) + b, \quad (3)$$

where  $a$  and  $b$  are normalization parameters,  $x_{\text{max}}$  is the maximum cutoff parameter. The results of the log-normal model (dashed lines) are calculated with  $N_{\text{LN}}(> x)$  and the

corresponding best-fit parameters, where

$$N_{\text{LN}}(> x) = H \cdot \left( \frac{1}{2} - \frac{1}{2} \operatorname{erf} \left( \frac{\log x - \mu}{\sqrt{2}\sigma} \right) \right), \quad (4)$$

where  $H$  is a normalization parameter, erf is the error function. One can see that both the power-law and log-normal models match the data well.

The statistical criterion for model selection is Akaike information criterion (AIC) or Bayesian information criterion (BIC). Generally, AIC and BIC are respectively written as  $\text{AIC} = 2k + C$  and  $\text{BIC} = k \ln(n) + C$ , where  $k$  is the number of model parameters,  $n$  is the number of data, and  $C \equiv -2 \ln L$ . In our case, AIC is used as the criterion for the model selection, because  $n$  is identical in the fits of the models. As shown in Table 3, the AIC values for the power-law model are smaller than those for the log-normal model, which means that the power-law model is better.

To access the goodness-of-fit for the power-law model, we perform the parametric bootstrap method for the power-law model (e.g., Yuan et al. 2018). We simulate 1000 data sets using the best-fit parameters of the power-law model, and obtain the best-fit values of  $C$  from those simulated data. The results are shown in Figure 5. One can see that the number fraction with  $C$  smaller than that of the actual data is  $< 95\%$  for the distributions of CORE/ $T_{\text{fl}}$ , HST-1/ $T_{\text{fl}}$  and HST-1/ $I_p$ . This suggests that the three distributions are well described by the power-law model. While the fraction is 97.5% for CORE/ $I_p$  distribution, which means a worse fitting.

#### 3.2 Correlation of light curves

A frequently used method for the correlation analysis is the discrete correlation function (DCF, Edelson & Krolik 1988). For two evenly sampled light curves, the significance level of the estimated correlation coefficients by DCF can be evaluated by the simulation of light curves using the corresponding power spectrum density (PSD). The light curve simulation technique was proposed by Timmer & Koenig (1995) and improved by Emmanoulopoulos et al. (2013). However, it is difficult to obtain the correct PSD for an unevenly sampled light curve. Kelly et al. (2014) have proposed a flexible approach to characterize the PSD for irregularly sampled variability. The light curve can be fitted by using the continuous-time autoregressive moving average (CARMA( $p, q$ )) model. Thereafter, the corresponding PSD can be expressed as the sum of Lorentzian functions with the best-fitting parameters. The significance levels can be estimated for the case of unevenly sampled data with the relatively accurate PSD. The DCF results are shown in Fig. 6. A strong correlation can be observed among the intensity light curves of the CORE and HST-1, with a significance of  $> 3\sigma$ .

## 4 DISCUSSION AND CONCLUSIONS

Using the *Chandra* observations, we study the statistical properties of the X-ray flares from CORE and HST-1 in M87 jet. 14 flares and 9 flares are extracted from the CORE and HST-1 light curves, respectively. We use the power-law and log-normal models to fit the distributions of  $I_p$  and  $T_{\text{fl}}$  in

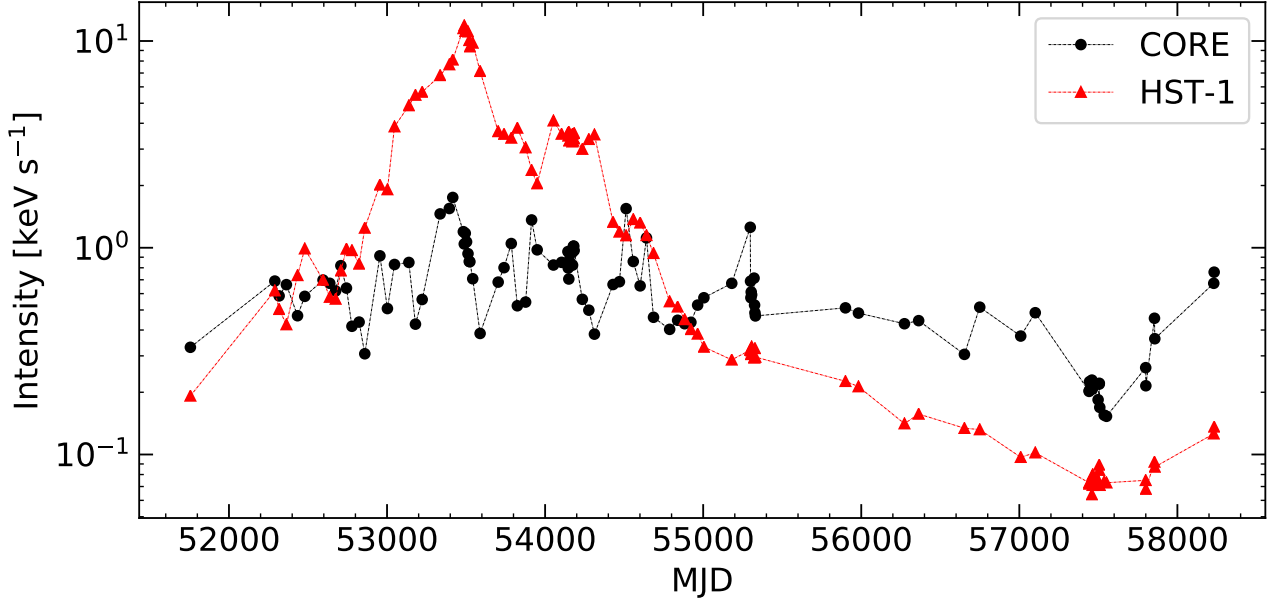


**Figure 3.** The light curves of the CORE (black filled circles) and HST-1 (red filled triangles). The data points are extracted from the regions shown in Fig. 1 and listed in Table 1.

**Table 2.** Identified flares of the CORE and HST-1. The start, peak, and end times are MJD. The peak intensity ( $I_p$ ) is in units of  $\text{keV s}^{-1}$ . The Col. Type demonstrates the specified parts that are used to identify the flares. See the text for the details of the identification procedures and the explanations for the symbols.

CORE					HST-1				
StartTime	PeakTime	EndTime	$I_p$	Type	StartTime	PeakTime	EndTime	$I_p$	Type
51755.8626	52290.0596	52317.3773	0.69	r	51755.8626	52290.0596	52363.3173	0.62	r
52859.1866	52954.8237	53002.4067	0.914	r	52363.3173	52479.5977	52674.5988	0.989	r
53179.7685	53415.7809	53488.5846	1.751	r	52823.3845	52954.8237	53002.4067	2.014	r
53824.3926	53914.5883	54052.7045	1.363	r	53002.4067	53488.5846	53494.957	11.872	r
57800.3854	57854.9918	57857.0845	0.456	r	53949.8696	54052.7045	54104.0902	4.114	r
52674.5988	52707.8893	52777.9248	0.819	d	53524.147	53542.069	53785.9837	9.783	d
53002.4067	53138.1528	53179.7685	0.849	d	54235.4596	54312.0629	54512.4793	3.522	d
53488.5846	53494.957	53588.7316	1.175	d	54512.4793	54557.8182	55180.8423	1.372	d
54173.5982	54181.159	54312.0629	1.019	d	55325.111	55327.4702	56273.284	0.326	d
54601.1848	54641.2694	54787.9406	1.116	d					
57008.7722	57100.8324	57441.5273	0.485	d					
53588.7316	53785.9837	53824.3926	1.048	m					
54312.0629	54512.4793	54601.1848	1.546	m					
54882.9431	55297.8852	55301.856	1.256	m					

**Table 3.** The best-fit results of power-law and log-normal. (1) two emission regions, (2) the distribution to be fitted, (3) power-law index, (4) minimum  $-2\ln L$  of power-law fit, (5-6) two parameters of log-normal model, (7) minimum  $-2\ln L$  of log-normal fit.

		power-law		log-normal		
		$\alpha$	$-2\ln L$	$\mu$	$\sigma$	$-2\ln L$
(1)	(2)	(3)	(4)	(5)	(6)	(7)
CORE	$T_{fl}$	$0.73^{+0.39}_{-0.37}$	171.38	$5.30 \pm 0.18$	$0.68^{+0.17}_{-0.12}$	175.17
	$I_p$	$0.69^{+0.39}_{-0.45}$	6.90	$-0.03 \pm 0.11$	$0.42^{+0.10}_{-0.07}$	12.06
HST-1	$T_{fl}$	$1.19^{+0.64}_{-0.60}$	116.93	$5.90 \pm 0.24$	$0.70^{+0.25}_{-0.16}$	122.67
	$I_p$	$0.92 \pm 0.32$	36.64	$0.76 \pm 0.46$	$1.36^{+0.49}_{-0.30}$	42.13

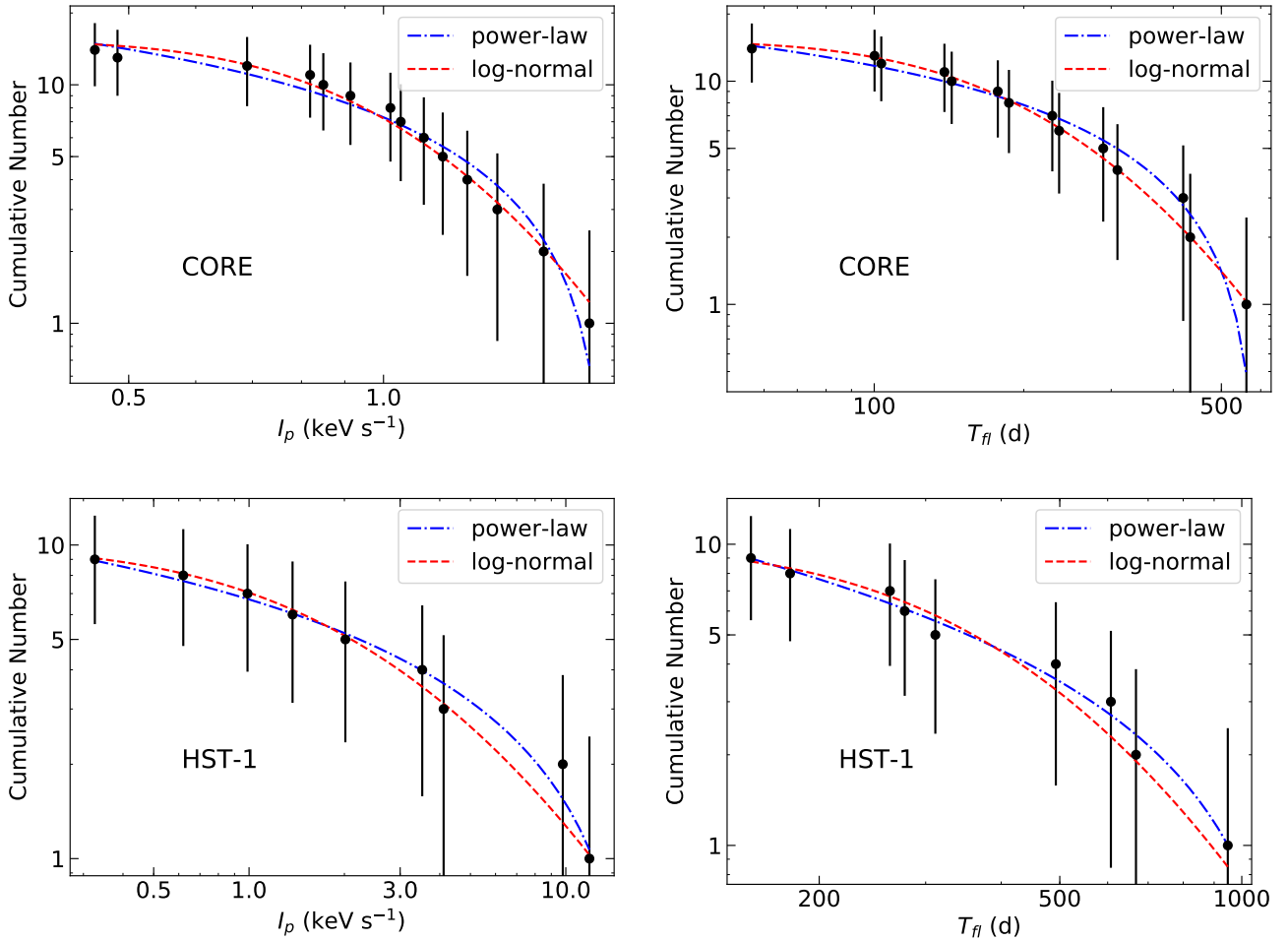


**Figure 4.** Comparison of the best-fit results and the data  $I_p/T_{fl}$ . Errors of the data points are at  $1\sigma$  level. The dash-dotted and the dashed lines are the best-fit results of the power-law and log-normal models, respectively. See the text for details.

the two regions. The results show that both models can fit the data well. While, the statistical criteria suggests that the power-law model is the better one. We furthermore examine the goodness-of-fit of the power-law model via bootstrapping sampling, and the results show that the data can be well characterized by the power-law model. Note that the fit to the CORE/ $I_p$  distribution by the power-law model is not very well. More data are needed to examine this distribution.

It has been proposed that the statistical properties of astrophysical X-ray flares from black hole systems can be explained by a fractal-diffusive SOC model (e.g., Wang & Dai 2013; Wang et al. 2015; Li et al. 2015; Yan et al. 2018). The SOC model expects that the distributions of event parameters, such as  $I_p$  and  $T_{fl}$  follow a power-law distribution. The corresponding indices can be expressed as  $\alpha_F = 1 + (S-1)/D_S$ , where  $D_S$  is the fractal Hausdorff dimension, spanning from 1 to  $S$ , and  $\alpha_T = 1 + \beta(S-1)/S$ , where  $\beta$  is a diffusion parameter (e.g., Aschwanden 2012). Here  $S$  is the spatial dimension of the energy dissipation domain.

Wang et al. (2015) investigated the statistical properties of 18 X-ray flares from the CORE in the M87 jet, and argued that SOC system with  $S = 3$  could explain the statistical

properties. We find that both the distributions of  $I_p$  and  $T_{fl}$  in CORE obey a power-law form, with the index  $\alpha_F = 0.69^{+0.59}_{-0.45}$  and  $\alpha_T = 0.73^{+0.39}_{-0.37}$ . Our results are consistent with Wang et al. (2015) within the errors.

Furthermore, it is found that both the distributions of  $I_p$  and  $T_{fl}$  in HST-1 also obey a power-law form, with  $\alpha_F = 0.92 \pm 0.32$  and  $\alpha_T = 1.19^{+0.64}_{-0.60}$ . Each index is consistent with that in the CORE within the errors.

It is noted that the uncertainties of the power-law indices are large, which is caused by the small number of the flares. More flares are needed to confirm the present results.

The statistical results of the CORE and HST-1 X-ray flares agree with the SOC model. This indicates that the X-ray flares in the CORE and HST-1 are possibly triggered by the magnetic reconnection, and the energy dissipation dimension was identical in the two regions. The strong correlation between the light curves in the CORE and HST-1 also hints that the flares in the two regions are triggered by the same mechanism. Our results support the argument that the magnetic reconnection is a natural process of energy dissipation in relativistic jets (e.g., Sironi et al. 2015; Singh et al. 2016).



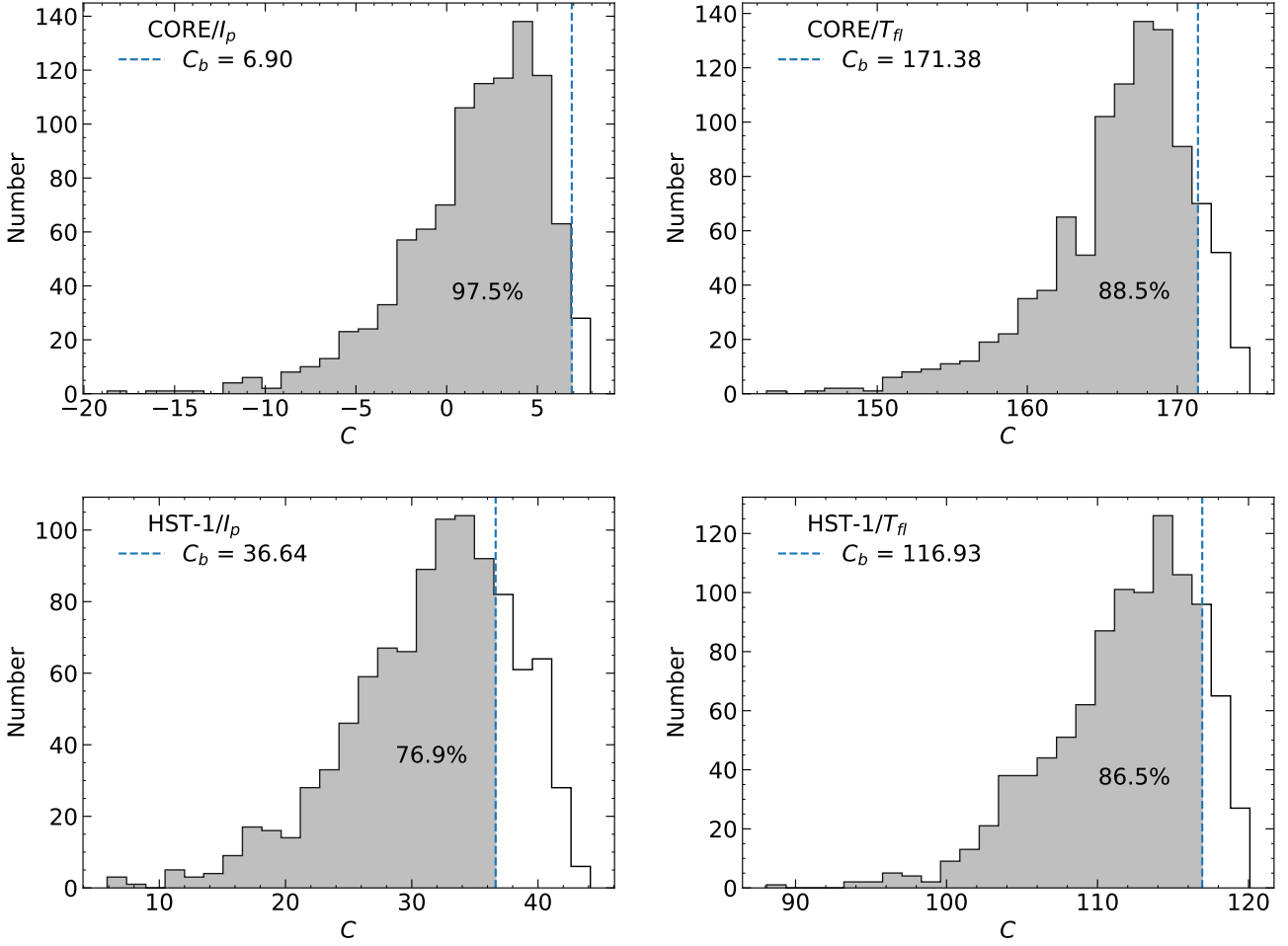


**Figure 5.** The goodness-of-fit for the best-fits of the power-law model. Distributions of the  $C$  (defined as  $C \equiv -2 \ln L$ ) value are calculated from the best-fits of the 1000 simulated data.  $C_b$  is the best-fit value for the real data.

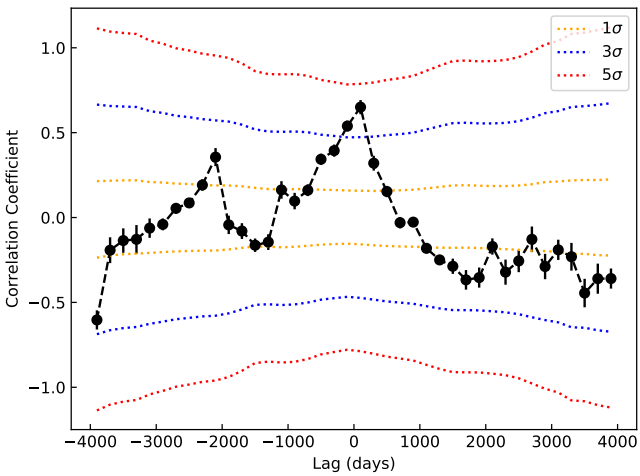


**Figure 6.** Result of DCF between the intensity light curves of the CORE and HST-1. The bin size of the DCF is 200 days. The orange, blue, and red dotted lines correspond to 1, 3, and 5 $\sigma$  significance levels, respectively.

Indeed, several models, including the current-driven (CD) kink instability and Kelvin-Helmholtz (KH) instability, have been proposed for the development of complex structures in astrophysical jets (Lyubarskij 1992; Bicknell & Begelman 1996; Begelman 1998). For blazars, the CD kink instability is believed to be the one occurring in the relativistic jets (Lyubarskij 1992; Begelman 1998; Lyubarskii 1999). The relativistic jet of M87 may induce similar CD kink instability, which is considered to be the driving mechanism behind the magnetic reconnection. The magnetic fluids suffer a CD kink instability within a short distance from the central engine. Hence, the jet is distorted by the instability, and structures such as knots are formed. Consequently, the distorted or disrupted magnetic field structures may trigger the magnetic reconnection process (e.g., Singh et al. 2016). The energy of the jet will be dissipated by converting the magnetic energy to the kinetic energy of the emitting particles.

**ACKNOWLEDGEMENTS**

We thank the anonymous referee for the constructive comments and suggestions. We acknowledge financial support from National Key R&D Program of China under grant No. 2018YFA0404204 and the National Natural Science Foundation of China (NSFC-11803081, NSFC-U1738124, NSFC-11573060, NSFC-11661161010, NSFC-U1531131). The work of D. H. Yan is also supported by the CAS “Light of West China” Program and Youth Innovation Promotion Association. S. Yang acknowledges the support from Yunnan Provincial Education Office Scientific Research Foundation Project (2019Y0023).

**REFERENCES**

- Aschwanden M. J., 2011, *Sol. Phys.*, **274**, 99  
 Aschwanden M. J., 2012, *A&A*, **539**, A2  
 Begelman M. C., 1998, *ApJ*, **493**, 291  
 Bicknell G. V., Begelman M. C., 1996, *ApJ*, **467**, 597  
 Biretta J. A., Zhou F., Owen F. N., 1995, *ApJ*, **447**, 582  
 Biretta J. A., Sparks W. B., Macchetto F., 1999, *ApJ*, **520**, 621  
 Davis J. E., 2001, *ApJ*, **562**, 575  
 Edelson R. A., Krolik J. H., 1988, *ApJ*, **333**, 646  
 Emmanoulopoulos D., McHardy I. M., Papadakis I. E., 2013, *MNRAS*, **433**, 907  
 Gebhardt K., Thomas J., 2009, *ApJ*, **700**, 1690  
 Harris D. E., Biretta J. A., Junor W., Perlman E. S., Sparks W. B., Wilson A. S., 2003, *ApJ*, **586**, L41  
 Harris D. E., Cheung C. C., Biretta J. A., Sparks W. B., Junor W., Perlman E. S., Wilson A. S., 2006, *ApJ*, **640**, 211  
 Harris D. E., Cheung C. C., Stawarz L., Biretta J. A., Perlman E. S., 2009, *ApJ*, **699**, 305  
 Harris D. E., et al., 2011, *ApJ*, **743**, 177  
 Kelly B. C., Becker A. C., Sobolewska M., Siemiginowska A., Uttley P., 2014, *ApJ*, **788**, 33  
 Li Y.-P., et al., 2015, *ApJ*, **810**, 19  
 Lu E. T., Hamilton R. J., 1991, *ApJ*, **380**, L89  
 Lyubarskii Y. E., 1999, *MNRAS*, **308**, 1006  
 Lyubarskij Y. E., 1992, *Soviet Astronomy Letters*, **18**, 356  
 Macchetto F., Marconi A., Axon D. J., Capetti A., Sparks W., Crane P., 1997, *ApJ*, **489**, 579  
 Marshall H. L., Miller B. P., Davis D. S., Perlman E. S., Wise M., Canizares C. R., Harris D. E., 2002, *ApJ*, **564**, 683  
 Perlman E. S., Harris D. E., Biretta J. A., Sparks W. B., Macchetto F. D., 2003, *ApJ*, **599**, L65  
 Singh C. B., Mizuno Y., de Gouveia Dal Pino E. M., 2016, *ApJ*, **824**, 48  
 Sironi L., Petropoulou M., Giannios D., 2015, *MNRAS*, **450**, 183  
 Sun X.-N., Yang R.-Z., Rieger F. M., Liu R.-Y., Aharonian F., 2018, *A&A*, **612**, A106  
 Timmer J., Koenig M., 1995, *A&A*, **300**, 707  
 Wang F. Y., Dai Z. G., 2013, *Nature Physics*, **9**, 465  
 Wang F. Y., Dai Z. G., Yi S. X., Xi S. Q., 2015, *ApJS*, **216**, 8  
 Weisskopf M. C., Tananbaum H. D., Van Speybroeck L. P., O’Dell S. L., 2000, in Truemper J. E., Aschenbach B., eds, *Proc. SPIE Vol. 4012, X-Ray Optics, Instruments, and Missions III*. pp 2–16 ([arXiv:astro-ph/0004127](https://arxiv.org/abs/astro-ph/0004127)), [doi:10.1117/12.391545](https://doi.org/10.1117/12.391545)  
 Wilson A. S., Yang Y., 2002, *ApJ*, **568**, 133  
 Yan D., Zhang L., Yuan Q., Fan Z., Zeng H., 2013, *ApJ*, **765**, 122  
 Yan D., Zhang L., Zhang S.-N., 2015, *MNRAS*, **454**, 1310  
 Yan D., Yang S., Zhang P., Dai B., Wang J., Zhang L., 2018, *ApJ*, **864**, 164  
 Yi S.-X., Xi S.-Q., Yu H., Wang F. Y., Mu H.-J., Lü L.-Z., Liang E.-W., 2016, *ApJS*, **224**, 20

Yuan Q., Wang Q. D., Liu S., Wu K., 2018, *MNRAS*, **473**, 306  
 Zhang J., Bai J. M., Chen L., Liang E., 2010, *ApJ*, **710**, 1017

This paper has been typeset from a  $\text{\TeX}/\text{\LaTeX}$  file prepared by the author.